Tellus (1991), *43A*, 37–48

Cloud albedo control by cloud-top entrainment

By HOWARD P. HANSON, *Atmospheric and Climate Dynamics Program, Cooperative Institute for Research in Environmental Sciences, University of Colorado at Boulder, 80309-0216, USA*

(Manuscript received 11 December 1989; in final form 2 May 1990)

ABSTRACT

Marine stratus and stratocumulus clouds exert a considerable influence on the Earth's heat budget, mainly due to their high albedos relative to the ocean surface. It is therefore important to understand the processes that control the radiative properties of these extensive cloud systems, particularly during daylight hours. Aircraft measurements of a stratocumulus cloud deck taken around local noon during the 1987 field phase of the First International Satellite Cloud Climatology Project Regional Experiment are the topic of this paper. A mixing line analysis of data from a series of flight tracks across a strong gradient in cloud albedo provides evidence that variations in the water vapor content of the air above the marine inversion can be responsible for the albedo change. The implications of this unexpected result for climate modeling are discussed.

1. Introduction

The role of clouds in the global climate system, particularly their potential for amplifying or damping trace gas induced climate change, remains one of the greatest challenges for atmospheric research. Since Schneider (1972) systematically examined the interplay between the changes in the solar and infrared (IR) heat budgets of Earth associated with variable cloud cover and cloud-top height, the problem for climate modelers has been to *predict* this variability. Because there are a wide variety of types of clouds, with a wide variety of processes controlling them, this is a problem of considerable complexity. One approach that has been adopted with some success in recent years has been to model the different types of clouds according to these controlling processes. Thus, for example, stratus and stratocumulus clouds in the marine atmospheric boundary layer (MABL) are treated using models of boundary-layer turbulence ranging from the simple mixed-layer approach (Lilly, 1968; Schubert et al., 1979a, b) through turbulence closure models of varying complexity (Oliver et al., 1978; Chen and Cotton, 1983) to large-eddy simulations (Deardorff, 1980a, b; Moeng, 1986). By focusing on the processes thought to be most important in controlling these clouds (in this case, radiation and turbulent transfer), progress toward improved models has been continuing.

Model studies, however, require observations for their verification, and, recently, there has been undertaken an ambitious program of combined field and theoretical work aimed at understanding more fully the climatic implications of clouds. As a part of the ISCCP (the International Satellite Cloud Climatology Project), U. S. agencies have collaborated on the First ISCCP Regional Experiment (FIRE), the first phase of which focused on cirrus and marine stratocumulus clouds (Starr, 1987, and Albrecht et al., 1988, respectively). The intensive field observations of the stratocumulus component of FIRE, of concern in this paper, focused on the marine layer off the coast of California with a combined program of satellite, aircraft, balloon, and ground measurements for a period of about 3 weeks in July, 1987. Discussed here are certain aspects of measurements made by the NCAR Electra research aircraft on 16 July. These measurements suggest that the role of cloud-top entrainment in controlling the albedo of the clouds is quite strong, and they also indicate the sensitivity of the cloud albedo to relatively small variations in above-inversion water vapor.

The next section of the paper provides back-

ground, both for the behavior of stratocumulus clouds and for the experimental instrumentation. Then, the flight patterns and their relationship to satellite observations are presented to introduce the aircraft measurements. The measurements are summarized in the context of a mixing diagram, which clearly illustrates the importance of cloud-top entrainment. The concluding section then discusses implications of these findings for cloud models, with emphasis on climatic implications.

2. Background

2.1. The cloud-topped MABL

The articles cited above provide ample introduction to the climatology and mechanics of the stratocumulus-topped MABL (the Schubert et al. papers are particularly instructive), but it is worthwhile here to summarize briefly conditions and processes with emphasis on more recent findings of relevance. The interactive relationships of radiative transfer and turbulence are especially important.

From a climatological perspective, the most persistent stratus and stratocumulus decks occur on the east sides of the subtropical high pressure ridges of the Atlantic and Pacific (in both northern and southern hemispheres), off the coasts of California and northern Mexico, Chile and Peru, Morocco and Western Sahara, and Angola and Namibia (Hanson, 1990). The equatorward flow, with a considerable easterly component (the beginning of the trades), is associated with low-level divergence, implying subsidence in the atmosphere and with off-shore Ekman drift, implying coastal upwelling, in the underlying oceans. The MABL forms between the cool, upwelled ocean water and the relatively warm, stable free atmosphere subsiding from above. The interface between the MABL and the free atmosphere is the marine inversion, which is generally, but not always, characterized by very strong stability and a sharp decrease in water content. If the MABL turbulence is sufficiently energetic to maintain the MABL depth at a level higher than the lifting condensation level, clouds form, often stratus and/or stratocumulus cloud decks of considerable areal extent. (The specific reasons for the formation of stratus versus stratocumulus versus trade cumulus are still not well understood and will be the topic of the second phase of FIRE.) Because these cloud decks are opaque to infrared radiation, they radiate nearly as blackbodies; there is therefore a strong radiative cooling off their tops, and this assists in maintaining the energetics of the turbulence. They are also, of course, quite reflective in the solar spectrum, and this shades the underlying ocean, helping to maintain the cool sea-surface temperatures.

The clouds also absorb solar radiation, and this impedes the maintenance of the turbulence energetics (Hanson, 1987b). One of the most important findings of recent years has been the radiatively induced separation of the MABL near or below cloud base (Nicholls, 1984; Turton and Nicholls, 1987; Nicholls, 1989). In this circumstance, the MABL evolves from a single well-mixed layer into two decoupled layers.

This happens because the stabilizing effect on the upper (cloudy) part of the MABL by solar energy absorption in the clouds can prevent surface-based turbulence from penetrating into the cloud layer. Often, a weak inversion (known as the transition layer, in trade cumulus situations) forms near cloud base. The lower part of the MABL remains turbulent, although at a lower level of energy than previously. The cloud layer is also turbulent, but its energetics and thermodynamic budgets are drastically altered. The water budget, in particular, no longer has the surface-flux source term to supply the cloud against entrainment of dry air from above. This leads to a thinning of the cloud and, frequently, its breakup. Because the absorption of solar energy increases monotonically with increased cloud water, there is a net negative feedback in this interplay of processes, and, due to the time-dependence associated with the diurnal cycle, the clouds can persist until sunset. At this time, the cloud-top infrared cooling generates turbulence energy with sufficient strength to re-couple the cloud and subcloud layers, and the surface moisture supply for the cloud resumes. Overnight, the well-mixed MABL reforms, and the thickest clouds occur just after sunrise.

However, because the climatic relevance of low-level stratocumulus and stratus clouds is their effect on the budget of solar radiation, it is their albedo during the daylight hours, when they undergo the decoupling process, that is important. Because the water budget during this time can be

dominated by the entrainment at cloud top, it is necessary to understand how this affects the clouds' radiative properties. The remainder of this paper deals with one set of observations that shows how sensitive the decoupled cloud can be to small variations in cloud-top entrainment.

2.2. *Mission 197-A of FIRE*

The 1987 FIRE marine stratocumulus intensive field operations program was conducted off the coast of southern California, with boundary-layer research aircraft based in San Diego and with surface observations made from San Nicolas Island, a U. S. Navy facility about 100 km west of Los Angeles (Albrecht et al., 1988). On 16 July (the 197th day of 1987), the NCAR Electra performed a research mission designed to allow instrumental intercomparisons with the surface-based equipment on San Nicolas. The flight pattern consisted of a series of level turbulence-measuring runs in and above the MABL (i) between San Nicolas and the R/V Pt. Sur, on station about 50 km to the WNW, and (ii) at, approximately, a right angle to (i) crossing at the midpoint (Fig. 1). It is the second set of flight legs that are of concern here; they are summarized in Table 1.

In terms of the way-points on Fig. 1, the pattern

Table 1. *Flight legs analyzed*

Leg #	Altitude (m)	Direction (°)	Comment
10	1600	200	lidar run above cloud
11	900	20	cloud-top "porpoise" run
12	750	200	middle of cloud layer
13	475	20	just above cloud base
14	50	200	near-surface fluxes

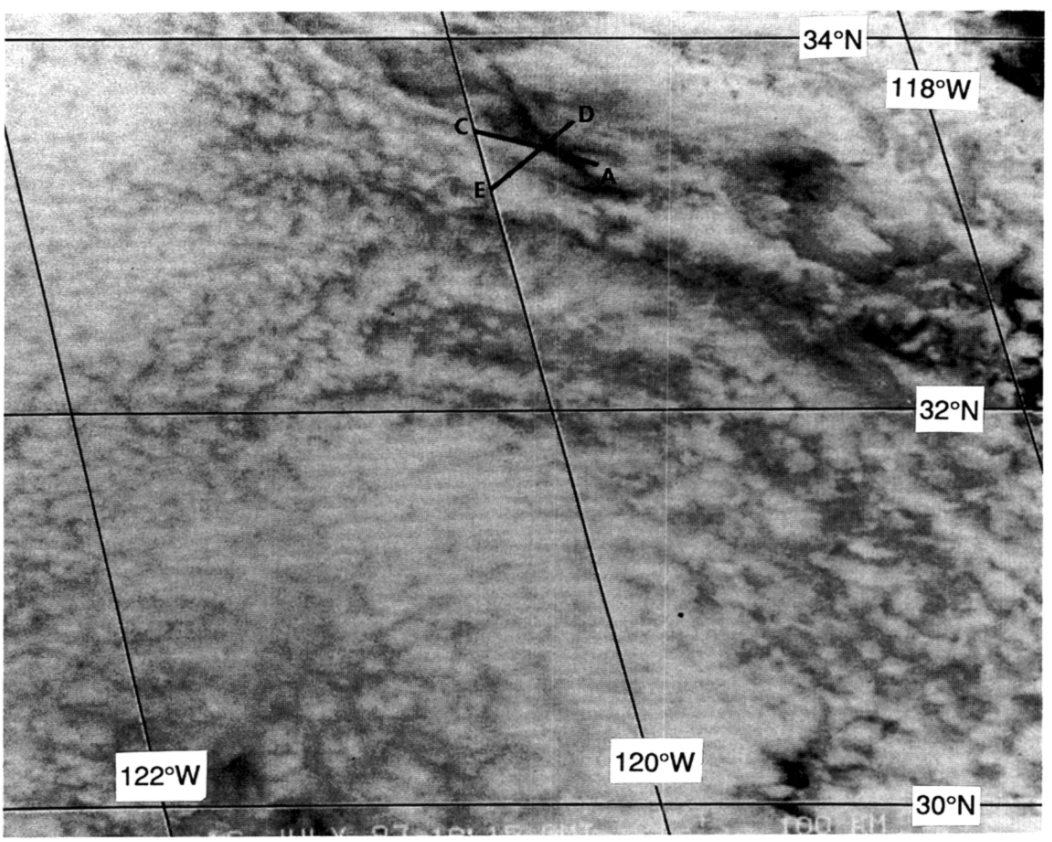

Fig. 1. Portion of GOES visible image, from 18:15 GMT on 16 July 1987, showing Electra flight tracks over the stratocumulus deck off the coast of California. Flight legs analyzed here occurred between way-points D and E.

of interest, then, took place between D and E. Notice that the appearance of the cloud in Fig. 1 changes dramatically at about the midpoint of this leg: the half-leg toward point D is considerably darker than that toward point E. This mission was coordinated with a LANDSAT IV overpass at 1104 local time, and the LANDSAT visible imagery shows that the dark part of the cloud had an albedo of about 0.4, while the brighter part had an albedo of about 0.6. It is this variability that is of interest here.

NCAR Electra instrumentation used in this analysis is, with one exception, confined to the standard meteorological, radiation, turbulence, and microphysics packages (e.g., Lenschow et al., 1988; Albrecht et al., 1988). Temperatures and dew points were measured (at 1 Hz) by Rosemont thermometers and by a dew-point mirror, respectively, and cloud liquid water was measured by a King hot-wire probe. Upward and downward solar and infrared broadband fluxes were measured with Eppley pyranometers and pyrgeometers, respectively; in addition, upward- and downward-looking Barnes radiometers measured the radiating temperature in the water vapor window. Fast-response turbulence measurements were obtained from a pitot tube and horizontal and vertical vanes on the nose boom (for the three wind components) and from a fast-response (NCAR K-probe) thermistor and a Lyman-α hygrometer. The analysis in this paper is concerned with the thermodynamics of the clouds, and various combinations of the temperature and moisture sensors were used to test the results for instrumental errors. The conclusions discussed below are essentially independent of which set of instruments is used in the analysis. A more detailed analysis of this data set, particularly one using the fast-response data, would require that the instruments be carefully corrected (Betts and Boers, 1990).

In addition to these standard instruments, the Electra also carried a steerable 10.3 μm lidar system, used to obtain cloud heights (Schwieschow, 1987). The penetration of the laser into clouds can also be used to infer cloud water density, but this technique is not used in this paper.

3. Analysis

This paper ultimately focuses on measurements made during the cloud-top "porpoise" run, Leg 11 in Table 1. These measurements provide the most revealing look at the processes responsible for the albedo variations shown in Figure 1. Before examining Leg 11 in detail, it is useful to summarize data from other legs, in order to provide background for discussing the cloud-top measurements.

3.1. Cloud liquid water content

Fig. 2 presents time series of data from Leg 10, obtained at 1600 m, well above the cloud deck. The approximate airspeed of the Electra, 100 m s^{-1}, can be used to translate the time scale at the bottom of the figure into distance. Shown are (top to bottom) temperature of the upwelling radiation in the water vapor window $T\uparrow$ (measured by a Barnes PRT-5 radiometer); downwelling solar radiation $F_{\text{sol}}\downarrow$ (calculated as the sum of measurements from 2 Eppley pyranometers covering the ultraviolet to the near infrared); cloud-top height z_{top} (calculated from the difference of the aircraft altitide and the range measurements from the infrared lidar); and the albedo α (calculated from the ratio of the upwelling solar radiation $F_{\text{sol}}\uparrow$ to $F_{\text{sol}}\downarrow$). The two segments of approximately 20 km labeled on the α trace are coincident with the albedo differences shown in Fig. 1. As mentioned, the quantitative differences in Fig. 1 are similar to those inferred from the LANDSAT scene obtained about 1 hr before this flight leg. The downwelling solar radiation is relatively constant over the two segments of interest, indicating that it is changes in the underlying stratocumulus cloud deck that are causing the albedo variability.

Note that the overall trends of the $T\uparrow$ and z_{top} time series coincide; that is, the upwelling radiation is warmer where the cloud top is *higher*. Because the actual cloud-top temperature decreases monotonically with height, this suggests that the cloud is thinner for segment 1, and that the PRT-5 is "seeing" radiation that is being transmitted through the cloud. That is, the emissivity of the cloud in segment 1 is less than unity. This is consistent with the time series from Leg 12, in the middle of the cloud layer (not shown), for which segment 1 liquid water measurements are near the noise level of the instruments. On the other hand, the liquid water mixing ratio for segment 2 of Leg 12 is 0.12 ± 0.03 g kg^{-1} (this is the average ± 1

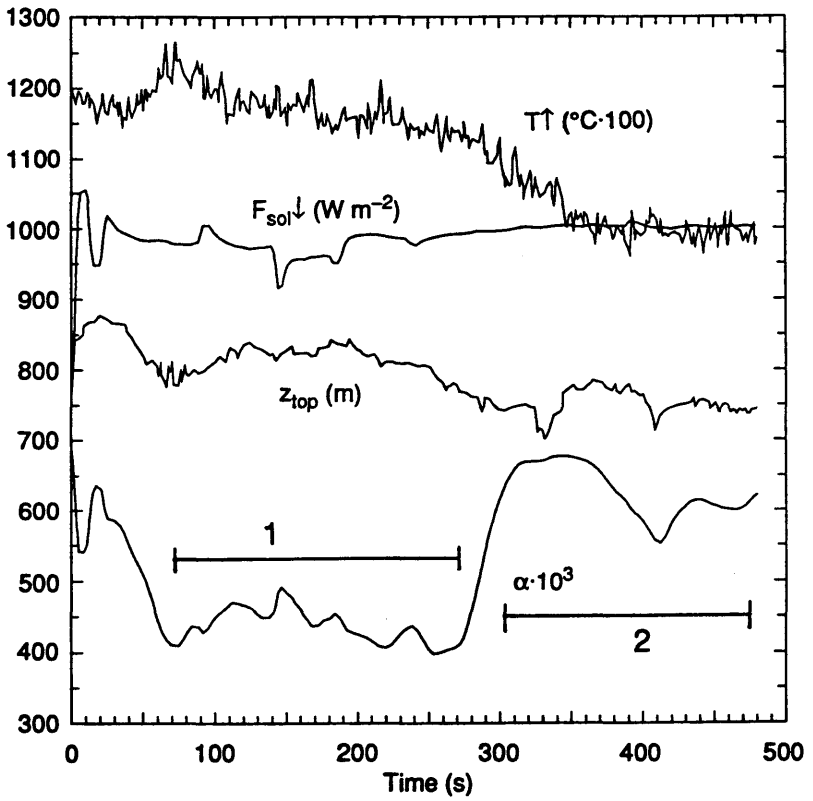

Fig. 2. Time series of (top to bottom) temperature of upwelling radiation in the water vapor window; downwelling solar radiation; cloud-top height; and cloud albedo, from Leg 10, at 1600 m.

standard deviation). The reason for the albedo difference and for the trend of the upwelling IR radiation between the two segments of Leg 10 is now apparent: the segment 1 part of the cloud was far thinner than the segment 2 part. If the albedos in Fig. 2 are used to invert the regression for albedo as a function of cloud liquid water path (LWP) developed by Coakley and Snider (1988, 1989), it is found that the segment 1 LWP is only about 25% of the segment 2 LWP. This is consistent with these differences in mid-cloud from Leg 12 when they are combined with the results from Leg 11 shown below.

Having established that the variability of the cloud's radiative properties from segment 1 to segment 2 was associated with differences in the total integrated liquid water content of the cloud, it remains to explain why the water content was so different in the two segments.

The argument advanced here is that this variability in the cloud water content was due to differences in water vapor content of the air above the cloud-top inversion. Entrainment by the cloud of this above-inversion air dried out the part of the cloud (in the sense of decreasing its liquid water content) associated with segment 1 much faster than it did for the part associated with segment 2.

There are two parts to this argument. The first involves showing that the cloud layer was cut off from the source of water vapor at the ocean surface, and therefore that radiative heating and entrainment were the only processes affecting the cloud layer. The second involves the details of the entrainment at the inversion.

3.2. Decoupling

There is ample evidence that the cloud and subcloud layers were decoupled, in the sense that there was relatively little turbulent exchange between them, during this mission. (It is important to note

that, in general, "decoupling" does not mean that the layers are completely isolated from each other—as with, for example, a material surface between them—but rather that turbulent exchange between the layers is small compared to that within each layer separately.) Albrecht and Barlow (1989) reported that FIRE measurements at San Nicolas Island, approximately 25 km to the ESE of the operations discussed here, indicated that the lifting condensation level for surface parcels was considerably lower than the cloud base height (as measured by a ceilometer) for the entire day in question. Turbulence measurements from the Electra, not shown here, reveal that the turbulent fluxes at the cloud-base level were very small, compared to those at other levels. Finally, the mixing diagram discussed below is also indicative of a decoupled MABL.

3.3. *Cloud-top entrainment*

Because the cloud layer was not receiving moisture from below, as is the usual case with well-mixed cloud-topped boundary layers, the variations in cloud water between segments 1 and 2 responsible for the albedo differences seen in Fig. 1 and 2 must be explained by differences in cloud-top entrainment and radiative heating. (The other candidate for variability is horizontal advection, but this was negligible on this day due to very low wind speeds. Parcel trajectories, during the part of the mission discussed here, were about the distance of the uncertainty in positioning the aircraft for the repeated legs in the stack.) Because of the limited amount of data, it is not possible to construct unambiguous thermodynamic budgets for the two Leg 11 segments, but it is possible, with the help of

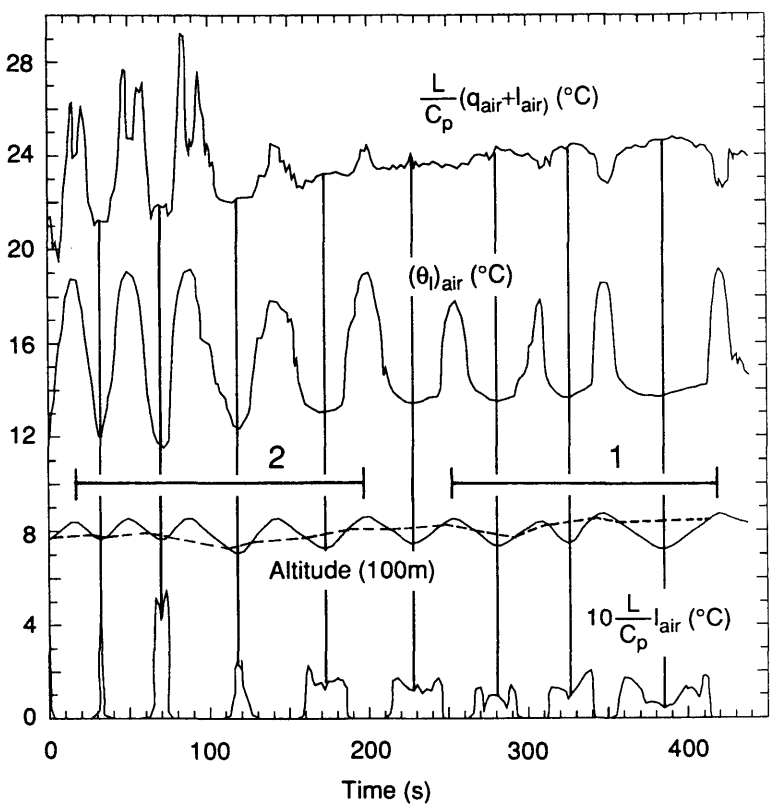

Fig. 3. Time series of (top to bottom) total water mixing ratio (in temperature units), liquid potential temperature, aircraft altitude (solid) and cloud top (dashed), and liquid water mixing ratio (in temperature units), from Leg 11, at cloud top. As indicated by the segment bars, the aircraft heading for this leg was opposite to that for Leg 10 (Fig. 2).

a mixing diagram, to develop a strong inference concerning the processes responsible for the cloud water variations.

Fig. 3 shows time series of several quantities of interest for the cloud-top leg. Note that this leg runs from way-point D to E (the opposite direction from Leg 10), so that the high-albedo segment (2) of the cloud is the *first* half or so of the leg. The time series of altitude (second from bottom, solid) shows the aircraft motion, hence the "porpoising" designation. The cloud liquid water content time series (bottom) from the King probe has been used to infer the cloud top height (the dashed curve superimposed on the altitude trace). Note that the mean aircraft altitude was maintained at an approximately constant level; therefore, toward the end of the leg, as the cloud-top height rose (see Fig. 2), the aircraft penetrated farther and farther into the cloud. The cloud liquid water content shows this clearly.

The top two time series in Fig. 3 are the total water mixing ratio (the sum of the King probe liquid water and the dew-point water vapor) at the top and the liquid potential temperature, second from top. The vertical lines superimposed on Fig. 3 indicate the low points of the porpoise maneuvers. The strength of the cloud-top temperature inversion, as measured by the liquid potential temperature, varies from about 7°C at the beginning of the leg to about 5°C at the end. While the temperature inversion is consistent with the expected structure of the boundary layer—warm air atop cold—the changes in water content are not. At the beginning of the leg (segment 2), there is actually more water (all vapor) in the air above the inversion than there is water (vapor plus liquid) in the cloud. As mentioned previously, this result is independent of the instruments used in the analysis, so this is not an instrumental artifact. In contrast, toward the end of the leg (segment 1), the more usual water content structure—with dry air above the inversion—begins to appear.

Fig. 3 implies that, in the first half of Leg 11 (the high-albedo part of the cloud), cloud-top entrainment is acting as a moisture source for the cloud, while in the second half of Leg 11, cloud-top entrainment is acting (weakly) to dry the cloud layer. This provides the second part of the argument that the variability of the cloud albedo in Figs. 1 and 2, which is related to the cloud liquid water path, is being controlled by variations in the water vapor content of the air above the cloud-top inversion. It remains to construct a coherent picture of the boundary layer as a whole for these flight legs.

3.4. *Mixing diagram*

The fundamental effect of boundary-layer turbulence is to mix together parcels of air of different properties (parcels associated with the thermodynamic states of the sea surface and the air above the boundary layer), forming in the process parcels of boundary-layer air. If S and U represent the properties of the surface air and the air above the boundary layer, respectively, the mixture M is, in the absence of non-conservative sources or sinks, simply $M=(1-f)U+fS$, where $0 \leqslant f \leqslant 1$ is the fraction of the mixture comprising the surface air. In a graphical sense, M lies on a line between S and U; this line is therefore a mixing line. *Mixing diagrams*, in which the properties S, U, and M represent more than one property (i.e., they are vectors), provide a powerful tool to summarize large amounts of data. Betts (1982, 1985) discussed mixing diagrams in detail in the context of saturation point analysis. Hanson (1984a) showed how mixing lines on such diagrams relate to the heat and moisture budgets of the cloud-topped boundary layer.

In Fig. 4, all the 1-second data from the boundary layer legs in Table 1 are presented on a mixing diagram that uses total water mixing ratio and liquid potential temperature as coordinates. While this coordinate system does not conserve energy in the manner of, say, a tephigram, it has the advantage that mixing lines are straight. The properties used, total water (i.e., liquid plus vapor) mixing ratio and liquid potential temperature are invariant upon water phase transformation between vapor and liquid. Data from Legs 13 and 14, the subcloud legs at 475 m and 50 m, respectively, are represented by the ellipses connected by the dashed line and the two ellipses to the left of that line. The center of each ellipse is the segment mean, and the axes of each ellipse represent ± 2 standard deviations of the segments. The ellipse labeled "S" represents the surface conditions—the ocean surface temperature, from the PRT-5 at 50 m, and the associated saturation mixing ratio. The small ellipse (for which the "1" and "2" are

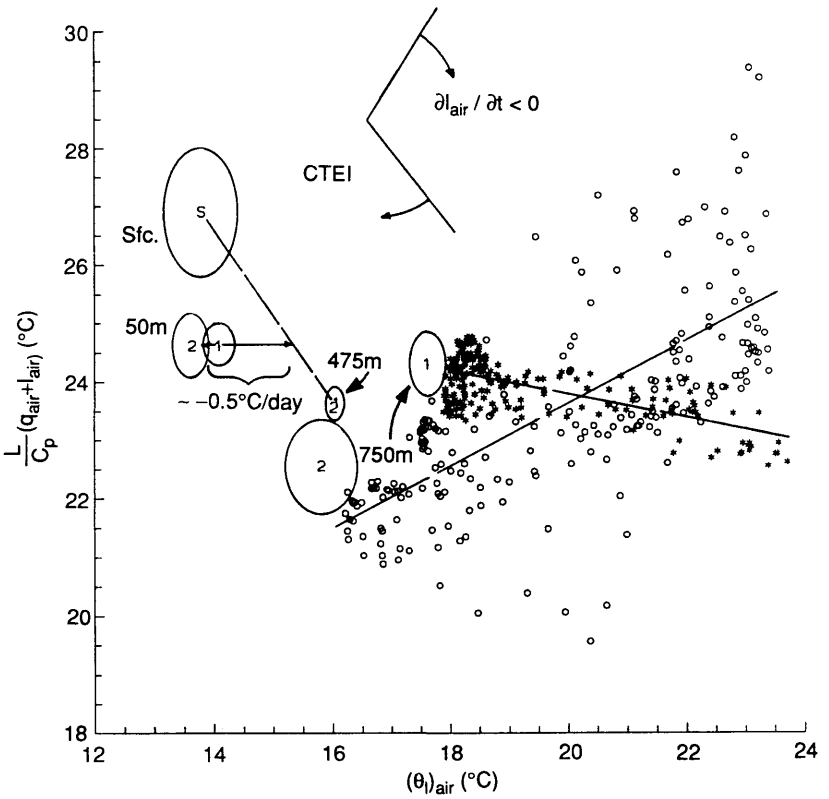

Fig. 4. Mixing diagram of data from Legs 11, 12, 13, 15 on 16 July 1987. Ellipses show the segment mean (center of ellipse) and ± 2 standard deviations; individual 1-second data points are for Leg 11 (the cloud-top leg), segment 1 (low albedo: asterisks) and segment 2 (high albedo: circles). See Section 3.4 for discussion.

superimposed) at the other end of the dashed line is the data from Leg 13 at 475 m (cloud base), and the two ellipses offset to the left are the 50-m data. The other two ellipses are the data from the segments of Leg 12, (at 750 m) and the individual 1-second data points are the data from the segments of Leg 11 at cloud top (the asterisks for segment 1 and the circles for segment 2). The two lines through these individual data points are least-squares regression fits.

3.4.1. Subcloud layer. Subcloud layer data are represented in Fig. 4 by the 3 sets of ellipses from the surface, 50 m and 475 m. Turbulent mixing occurs between the surface air and the air at cloud base, and, in the absence of other processes, subcloud layer parcels would fall along the (dashed) mixing line between the two. However, in the subcloud layer there is a background radiative cooling. The offset of the 50-m data points toward lower temperatures (at constant water mixing ratio) can be explained by a radiative cooling rate of 0.5°C day^{-1} normalized by the net mixing rate determined from the surface transfer rate and the implied entrainment rate at the top of the subcloud mixed layer. The surface transfer rate is the product of the wind speed and the surface transfer coefficient C_T ($C_T = 1.4 \cdot 10^{-3}$ was used here); the entrainment rate was inferred by assuming that the downward buoyancy flux at the top of the subcloud layer was 20% of the (upward) surface buoyancy flux. That the 50 m data for the two segments are separated in the figure can be explained by a $\pm 25\%$ variation in the radiative cooling rate, which can be expected due to the differences in cloud cover over the two segments.

That the gross features of the subcloud layer can be explained in this fashion lends credence to the

decoupling argument discussed in Section 3.2, as does the radically different slope of the subcloud mixing line compared to the mixing lines in the cloud layer.

3.4.2. Cloud layer. The cloud layer data, the remaining two ellipses for the 750 m data from Leg 12 and the individual 1-second data points from Leg 11, represent mixing across the cloud top and within the upper part of the layer. The data for segment 1, the low albedo segment, are shown by the asterisks, and the linear regression of the Leg 11 data is almost precisely aligned with the Leg 12 data (the 750-m ellipse labeled "1"). That the regression line is nearly horizontal reflects the much larger variability of θ_l than of $q+l$ in Fig. 3. The segment 2 data (the circles) exhibit far more variability in $q+l$, as expected from Fig. 3. That the segment 2 data from Leg 12 lies at a higher water content than the cloud-top data (the left end of the regression line) suggests that there is redistribution within the cloud of water by drizzle, removing water from the cloud top and re-evaporating it lower down. It is also of interest that the segment 2 water content is lower than that for segment 1; however, since the temperature is also lower, there is actually more liquid water in segment 2, as seen in Fig. 3. This is consistent with the drizzle for segment 2 but not for segment 1.

Near the top of Fig. 4, the two mixing lines with arrows pointing clockwise indicate the limits of two mixing processes. The "CTEI" mixing line shows the cut-off of cloud-top entrainment instability mixing; mixing lines lying clockwise of this line are subject to this instability. Clearly, neither segment of Leg 11 is subject to CTEI.

The other line indicates the limit for which $\partial l/\partial t = 0$; mixing lines lying clockwise of this limit imply that the liquid water mixing ratio will decrease with time. This is derived in the Appendix; it is the mixing diagram version of Randall's (1984) cloud deepening by entrainment. For a given mixing rate, the more clockwise the mixing line, the faster the cloud liquid water decreases. This shows that the segment 1 liquid water was decreasing faster that the segment 2 liquid water. If it can be assumed that the entrainment rate was identical for the two segments, then it can be shown that the decrease for segment 1 was about 50% faster than for segment 2.

However, it is likely that the entrainment rate for segment 1 was greater than for segment 2, because the cloud-top is slightly higher for segment 1 than for segment 2 (Figs. 2 and 3). This implies even faster drying for segment 1. Such a difference in entrainment rates is consistent with the differences in the cloud thickness: the thicker cloud in segment 2 would be absorbing more solar radiation throughout the cloud's depth, causing greater heating and thus damping the turbulence kinetic energy (generated by cloud-top cooling and evaporation) more effectively than for segment 1 (Hanson, 1987a, b). This would lead to a lower entrainment rate. However, there is no way to quantify these differences with the limited data set available from the single aircraft used here.

4. Conclusions

Satellite images of marine stratocumulus clouds almost always show substantial variability in the clouds' radiative properties on a wide range of scales. As more is learned about these cloud systems, the processes responsible for these variations are becoming better understood. The process of cloud-top entrainment instability (Deardorff, 1980a; Randall, 1980; Hanson, 1984b; among others) has long been a candidate explanation of cloud-thickness variability. More recently, the role of cloud microphysics was discussed by Coakley et al. (1987), who showed how particulates from diesel powerplants on ships can act as cloud condensation nuclei and produce high-albedo "ship tracks" in the cloud decks.

This paper has discussed yet another mechanism that can produce variations of cloud radiative properties, entrainment of air with variable thermodynamic properties from above the cloud. The role played by above-inversion variability in the stability of the boundary layer has been discussed by Betts and Albrecht (1987) and by Betts and Ridgway (1988); the results presented here show that this influence also extends to cloud radiative properties. The FIRE data from 16 July 1987 suggest that variations of cloud albedo of the order of 50% (from ~ 0.4 to ~ 0.6) can be caused by variations of the water vapor above the cloud of only about $1.5\,\mathrm{g\,kg^{-1}}$. The reason for the variability of the above-cloud air is beyond the scope of this paper, but it is worth noting that trajectory analyses for this and other days during the

FIRE field work show that the combination of subsidence and flow around the subtropical high can lead to widely different origins for parcels having relatively close locations over the stratocumulus regime off California (Kloesel and Albrecht, 1989; Kloesel, 1989).

The importance of this finding lies both in its unexpected character and in its implications for climate modeling.

It is unexpected because the traditional view of the marine boundary layer is that it responds to changes in advection and the sea surface temperature, and that the relatively quiescent air above the inversion acts as a mainly passive lid, against which entrainment operates. Sensitivity to changes in the above-inversion air has been discussed (e.g., Schubert, 1976), but the main interest has been with the lower boundary and the changes in the radiative budget with the presence of clouds. This analysis has shown that the above-inversion air can, in certain circumstances, actually control the albedo of the boundary-layer cloud deck.

The implications of this finding for climate modeling are challenging, even distressing in the current state of the art. The albedo of marine stratocumulus clouds is a crucial component of the Earth's radiative heat budget, and predicting this albedo is very important both for diagnostic studies of the current climate and for the prediction of future climates. If small changes in water vapor above the boundary layer (changes of the order of 1-2 g kg^{-1}) can change the cloud albedo by as much as 50%, then the need for a precise calculation of the atmospheric moisture budget is paramount. Yet this is one of the weaker links in the chain of climate modeling. Moreover, the subsidence of air in the subtropical high along isentropes (the process that appears to be responsible for the variations discussed here) is simulated well only in especially formulated models (i.e., models using isentropic coordinates) and not at all well in the typical general circulation model, which uses some form of pressure coordinates.

5. Acknowledgments

This paper is the result of research supported by Contract No. NOOO-14-84-K-0405 from the Marine Meteorology Program, Office of Naval Research; Grant No. NAG-1-051 from the National Aeronautics and Space Administration's Langley Research Center; and by the National Science Foundation, which supports the National Center for Atmospheric Research, whose aircraft was used for this research.

The observations discussed here are the combined result of efforts from a large number of individuals on the FIRE Science Team; I particularly wish to express my gratitude to D. Wylie (especially for providing Fig. 1), B. Weilicki, R. Schwiesow, K. Kloesel, A. Betts (who provided a most useful review of the original manuscript) and B. Albrecht for their contributions, both in terms of data sets and intellectual stimulation, to this work.

6. Appendix

The $\partial l/\partial t = 0$ mixing line

The derivation of the slope of the $\partial l_{\text{air}}/\partial t = 0$ mixing line shown on Fig. 4 involves the definitions of r, the total water mixing ratio, θ_l, the liquid potential temperature, θ_e, the equivalent potential temperature, the Clausius-Claperyon equation, and the assumption that the mixing takes place at constant pressure. This assumption is valid for mixing across the small altitude range associated with the cloud-top data shown in Fig. 4. Although the exact definitions of liquid and equivalent potential temperature can be used, for graphical purposes here it is sufficient to linearize:

$$\theta_l \cong \theta - L/C_p l, \tag{A1}$$

where θ is the potential temperature, and L and C_p are the latent heat of condensation and the specific heat of air at constant pressure, respectively. In saturated conditions,

$$r = q^* + l \tag{A2}$$

where q^* is the saturation mixing ratio. Assuming that parcels in clouds remain just saturated (a common assumption in modeling studies), a thermodynamic constant Λ can be defined such that

$$\delta q^* = \Lambda\, \delta\theta, \tag{A3}$$

that is, small changes in saturation mixing ratio are proportional to small changes in potential temperature.

A linearized equivalent potential temperature θ_e is

$$\theta_e \cong \theta + L/C_p q^*, \tag{A4}$$

from which

$$\frac{L}{C_p}\delta q^* \equiv \Gamma\,\delta\theta_e \equiv \Gamma\left[\delta\theta_l + \frac{L}{C_p}\delta r\right], \tag{A5}$$

where

$$\Gamma \equiv \frac{L/C_p\Lambda}{1 + L/C_p\Lambda}. \tag{A6}$$

Since $l = r - q^*$, (A5) can be rearranged to give

$$\frac{L}{C_p}\delta l = \Gamma\,\delta\theta_l\left[\frac{1-\Gamma}{\Gamma}\frac{L/C_p\,\delta r}{\delta\theta_l} - 1\right]. \tag{A7}$$

Now, $\Gamma > 0$ always, and, for a statically stable inversion, $\delta\theta_l > 0$, that is, changes in the liquid potential temperature associated with entrainment will be positive. Therefore, $L/C_p\,\delta l \leqslant 0$ if and only if

$$\frac{L/C_p\,\delta r}{\delta\theta_l} \leqslant \frac{\Gamma}{1-\Gamma} \equiv \frac{L}{C_p}\Lambda. \tag{A8}$$

The Clausius-Claperyon equation gives

$$\frac{L}{C_p}\Lambda = \frac{\varepsilon L^2}{RC_pT^2}q^* \sim 1.6, \tag{A9}$$

where $\varepsilon = 0.622$ and T is temperature. This value is plotted in Fig. 4.

REFERENCES

Albrecht, B. A. and Barlow, R. A. 1989. Large-scale variability in marine stratocumulus clouds defined from simultaneous aircraft and satellite measurements. *Extended Abstracts*, FIRE Science Meeting, July 10–14, Monterey, CA, FIRE Project Office, NASA Langley Research Center, 10–13.

Albrecht, B. A., Randall, D. A. and Nicholls, S. 1988. Observations of marine stratocumulus clouds during FIRE. *Bull. Amer. Meteorol. Soc. 69*, 618–626.

Betts, A. K. 1982. Cloud thermodynamic models in saturation point coordinates. *J. Atmos. Sci. 39*, 2182–2191.

Betts, A. K. 1985. Mixing line analysis of clouds and cloudy boundary layers. *J. Atmos. Sci. 42*, 2751–2763.

Betts, A. K. and Albrecht, B. A. 1987. Conserved variable analysis of the convective boundary layer thermodynamic structure over the tropical oceans. *J. Atmos. Sci. 44*, 83–99.

Betts, A. K. and Ridgway, W. 1988. Coupling of the radiative, convective, and surface fluxes over the equatorial Pacific. *J. Atmos. Sci. 45*, 522–536.

Betts, A. K. and Boers, R. 1990. A cloudiness transition in a marine boundary layer. *J. Atmos. Sci. 00*, 000–000.

Chen, C. and Cotton, W. R. 1983. A one-dimensional simulation of the stratocumulus-topped mixed layer. *Boundary-Layer Meteorol. 25*, 289–321.

Coakley, J. A., Jr., Bernstein, R. L. and Durkee, P. A. 1987. Effect of ship-stack effluents on cloud reflectivity. *Science 237*, 1020–1022.

Coakley, J. A. and Snider, J. B. 1988. Dependence of marine stratocumulus reflectivities on liquid water paths. *Extended Abstracts*, FIRE Science Team Workshop, Vail, CO, July 7–11, FIRE Project Office, NASA Langley Research Center, 355–359.

Coakley, J. A. and Snider, J. B. 1989. Observed cloud reflectivities and liquid water paths—and update. *Extended Abstracts*, FIRE Science Meeting, Monterey, CA, July 10–14, FIRE Project Office, NASA Langley Research Center, 63–66.

Deardorff, J. W. 1980a. Cloud-top entrainment instability. *J. Atmos. Sci. 37*, 131–147.

Deardorff, J. W. 1980b. Stratocumulus-capped mixed-layers derived from a three-dimensional model. *Boundary-Layer Meteorol. 18*, 495–527.

Hanson, H. P. 1984a. On mixed-layer modeling of the stratocumulus-topped marine boundary layer. *J. Atmos. Sci. 41*, 1226–1234.

Hanson, H. P. 1984b. Stratocumulus instability reconsidered: A search for physical mechanisms. *Tellus 36A*, 355–368.

Hanson, H. P. 1987a. Reinterpretation of cloud-topped mixed-layer entrainment closure. *Tellus 39A*, 215–225.

Hanson, H. P. 1987b. Radiative/turbulent transfer interactions in layer clouds. *J. Atmos. Sci. 44*, 1287–1295.

Hanson, H. P. 1990. Marine stratocumulus climatologies. *Int. J. Climatol.*, in press.

Kloesel, K. A. 1989. The above-inversion moisture structure observed during FIRE. *Extended Abstracts*, FIRE Science Meeting, July 10–14, Monterey, CA, FIRE Project Office, NASA Langley Research Center, 51–55.

Kloesel, K. A. and Albrecht, B. A. 1989. Low-level inversions over the tropical Pacific: Thermidynamic structure of the boundary layer and the above-inversion moisture structure. *Mon. Weath. Rev. 117*, 87–101.

Lenschow, D. H., Paluch, I. R., Bandy, A. R., Pearson, Jr., R., Kawa, S. R., Weaver, C. J., Huebert, B. J., Kay, J. G., Thornton, D. C. and Driedger III, A. R. 1988. Dynamics and chemistry of marine stratocumulus (DYCOMS) experiment. *Bull. Amer. Meteor. Soc. 69*, 1058–1067.

Lilly, D. K. 1968. Models of cloud-topped mixed layers

under a strong inversion. *Quart. J. Roy. Meteor. Soc. 94*, 292–309.

Moeng, C.-H. 1986. Large-eddy simulation of a stratus-topped boundary layer. Part 1: Structure and budgets. *J. Atmos. Sci. 43*, 2886–2900.

Nicholls, S. 1984. The dynamics of stratocumulus: Aircraft observations and comparisons with a mixed layer model. *Quart. J. Roy. Meteorol. Soc. 110*, 783–820.

Nicholls, S. 1989. The structure of radiatively driven convection in stratocumulus. *Quart. J. Roy. Meteorol. Soc. 115*, 487–511.

Oliver, D. A., Lewellen, W. S. and Williamson, G. G. 1978. The interaction between turbulent and radiative transport in the development of fog and low-level stratus. *J. Atmos. Sci. 35*, 301–316.

Randall, D. A. 1980. Conditional instability of the first kind, upside-down, *J. Atmos. Sci. 37*, 125–130.

Randall, D. A. 1984. Stratocumulus cloud deepening through entrainment. *Tellus 36A*, 446–457.

Schneider, S. H. 1972. Cloudiness as a global climatic feedback mechanism: The effects on the radiation balance and surface temperature of variations in cloudiness. *J. Atmos. Sci. 29*, 1413–1422.

Schubert, W. A. 1976. Experiments with Lilly's cloud-topped mixed layer model. *J. Atmos. Sci. 33*, 436–446.

Schubert, W. H., Wakefield, J. S., Steiner, E. J. and Cox, S. K. 1979a. Marine stratocumulus convection. Part I: Governing equations and horizontally homogeneous solutions. *J. Atmos. Sci. 36*, 1286–1307.

Schubert, W. H., Wakefield, J. S., Steiner, E. J. and Cox, S. K. 1979b. Marine stratocumulus convection. Part II: Horizontally inhomogeneous solutions. *J. Atmos. Sci. 36*, 1308–1324.

Schwiesow, R. L. 1987. The NCAR airborne infrared lidar system (NAILS), design and operation. NCAR Technical Note 291 + 1A, June, 1987, 38 pp.

Starr, D. O'C. 1987. A cirrus-cloud experiment: Intensive field observations planned for FIRE. *Bull. Amer. Meteorol. Soc. 68*, 119–124.

Turton, J. and Nicholls, S. 1987. A study of the dirunal variation of stratocumulus using a multiple mixed layer model. *Quart. J. Roy. Meteorol. Soc. 113*, 969–1010.